

# Electrokinetic Transport in Nanochannels. 2. Experiments

Sumita Pennathur\* and Juan G. Santiago

Department of Mechanical Engineering, Stanford University, Stanford, California 94305

We present an experimental study of nanoscale electrokinetic transport in custom-fabricated quartz nanochannels using quantitative epifluorescence imaging and current monitoring techniques. One aim is to yield insight into electrical double layer physics and study the applicability of continuum theory to nanoscale electrokinetic systems. A second aim is to explore a new separation modality offered by nanoscale electrophoretic separations. We perform parametric variations of applied electric field, channel depth, background buffer concentration, and species valence to impose variations on  $\zeta$  potential, effective mobility, and Debye length among other parameters. These measurements were used to validate a continuum theory-based analytical model presented in the first of this two-paper series. Our results confirm the usefulness of continuum theory in predicting electrokinetic transport and electrophoretic separations in nanochannels. Our model leverages independent measurements of  $\zeta$  potential performed in a microchannel system at electrolyte concentrations of interest. These data yield a  $\zeta$  potential versus concentration relation that is used as a boundary condition for the nanochannel electrokinetic transport model. The data and model comparisons together show that the effective mobility governing electrophoretic transport of charged species in nanochannels depends not only on ion mobility values but also on the shape of the electric double layer and analyte ion valence. We demonstrate a method we term electrokinetic separation by ion valence, whereby both ion valence and mobility may be determined independently from a comparison of micro- and nanoscale transport measurements.

In nanometer-scale electrokinetic channels, electric double layer (EDL) thicknesses are comparable to characteristic channel dimensions. The velocity profile is highly nonuniform, resulting in a decreased net flow rate per unit cross-sectional area relative to the thin EDL case.<sup>1–16</sup> In the first of this two-paper series, we

presented a review of theoretical and experimental studies of electrokinetic transport in nanometer-scale fluidic channels.<sup>16</sup> We also presented analytical and numerical models for net streamwise transport of both neutral and charged analyte species within long, thin electrokinetic channels. We used a simple numerical integration technique to solve for the transverse potential,  $\Psi(y)$ , in conditions of both low and high  $\zeta$  potential. We considered the addition of a dilute analyte sample species S whose concentration is much lower than that of background electrolyte ions. We demonstrated that transverse electromigration is in quasi-equilibrium with transverse diffusion flux. This quasi-steady transverse concentration distribution couples with the nonuniform velocity profile of nanochannel electrokinetic transport to yield an observed, area-averaged species velocity,  $\langle u_S \rangle$ , of the form

$$\langle u_S \rangle = \frac{\epsilon E \zeta}{\mu} \left\langle \exp\left(\frac{-z_S e (\psi(y) - \psi_0)}{kT}\right) \left(1 - \frac{\psi(y)}{\zeta}\right) \right\rangle + \nu_S z_S F E \quad (1)$$

where  $F$  is Faraday's constant,  $\nu_S$  is the (typical) species mobility, and the operator  $\langle \rangle$  represents a transverse ( $y$ -direction) depth-averaged quantity of the form  $\langle \rangle = 1/(2h) \int_{-h}^h (\ ) dy$ . The channels used in our experiments have 20:1 width-to-depth aspect ratios and so velocity and potential fields can be approximated as functions of only the transverse dimension,  $y$ .<sup>16</sup> The operator  $\langle \rangle$  can therefore also be interpreted as an area-averaging operation. The term  $(1 - \psi(y)/\zeta)$  in eq 1 describes the shape of the velocity profile, and the product of this term and the exponential within the area operator describes the coupling between the velocity profile and the transverse concentration of the analyte of valence  $z_S$ . The resulting unsteady, two-dimensional species concentration field can then be expressed as

$$c_c(x, y, t) = \hat{c}_0 \frac{\exp(-(x - \langle u_S(x) \rangle t)^2 / 4Dt)}{\sqrt{4\pi Dt}} \times \exp\left(\frac{-z_S e (\psi(y) - \psi_0)}{kT}\right) \quad (2)$$

where  $t$  is time,  $x$  is the streamwise coordinate, and  $D$  is the (isotropic) molecular diffusion coefficient.

\* To whom correspondence should be addressed. E-mail: sumita@stanford.edu. Fax: (650)-723-7657.

- (1) Burgeen, D.; Nakache, F. R. *J. Phys. Chem.* **1964**, *68*, 1084–1091.
- (2) Dutta, P.; Beskok, A. *Anal. Chem.* **2001**, *73*, 1979–1986.
- (3) Datta, B.; McEldoon, J. P. *Anal. Chem.* **1992**, *64*, 227–223.
- (4) Datta, R.; Kotamurthi, V. R. *AIChE J.* **1990**, *36*, 916–926.
- (5) Conlisk, A. T.; McFerran, J. *Anal. Chem.* **2002**, *74*, 2139–2150.
- (6) Fulinski, A.; Kosinska, I. D.; Siwy, Z. *Europhys. Lett.* **2004**, *67*, 683–689.
- (7) Feng, J. J.; Krishnamoorthy, S.; Sundaram, S.; Bharadwaj, R.; Santiago, J. G. Computational Publications: Cambridge, MA, 2003; pp 234–237 vol.231.

- (8) Fang, C.; Wu, B.; Zhou, X. *Electrophoresis* **2004**, *25*, 375–380.
- (9) Griffiths, S.; Nilson, R. H. *Anal. Chem.* **1999**, *71*, 5522–5529.
- (10) Griffiths, S.; Nilson, R. H. *Anal. Chem.* **2000**, *72*, 4767–4777.
- (11) Rice, C. L.; Whitehead, R. J. *Phys. Chem.* **1965**, *69*, 417–424.
- (12) Levine, S.; Marriott, J. R.; Neale, G.; Epstein, N. J. *Colloid Interface Sci.* **1975**, *52*, 136–149.

The following relation highlights the effect of transverse electromigration and valence number on net streamwise electrophoretic transport in a nanochannel:<sup>16</sup>

$$\frac{\langle \nu_{S,\text{nano}} \rangle}{\nu_S} = 1 - \frac{1}{\beta} \left( \left( 1 - \frac{\psi(y)}{\zeta} \right) \left( \exp \left( \frac{-z_S e (\psi(y) - \psi_c)}{kT} \right) - 1 \right) \right) \quad (3)$$

where  $\langle \nu_{S,\text{nano}} \rangle$  and  $\nu_S$  are the effective electrophoretic mobility of a charged species in a nanochannel and a (thin EDL) microchannel, respectively.  $\nu_S$  is the usual ion mobility of a species defined as  $u_d/EFz_S$ , where  $u_d$  is the net drift velocity (i.e., relative to the local liquid velocity) for an ion of valence  $z_S$  subject to an electric field  $E$ .<sup>15</sup>  $\langle \nu_{S,\text{nano}} \rangle$  is an effective mobility parameter associated with a net drift velocity that is measured relative to the background area-averaged liquid velocity.  $\langle \nu_{S,\text{nano}} \rangle$  is defined as  $(\langle u_S \rangle - \langle u \rangle) / (EFz_S)$ , where  $\langle u_S \rangle$  is the observed, area-averaged velocity of the species and  $\langle u \rangle$  is the area-averaged velocity of the liquid in the channel.  $\langle \nu_{S,\text{nano}} \rangle$  is distinct from the common definition of electrophoretic mobility of an analyte in that it depends on both transverse ion electromigration and its coupling with a nonuniform electroosmotic velocity profile. The parameter  $\beta$  in eq 3 is the ratio of the electrophoretic velocity to the Helmholtz–Smoluchowski velocity for electroosmotic flow,  $\mu z_S \nu_S F / \epsilon \zeta$ . The ratio  $\langle \nu_{S,\text{nano}} \rangle / \nu_S$  can be interpreted as the factor by which electrophoretic mobility is apparently changed from the standard ion mobility value when the charged species is observed migrating through a nanochannel (where its net axial motion couples with the nonuniform velocity profile of the EDL). This ratio helps quantify the net change in streamwise electrophoretic flux due solely to nanochannel transport effects.

In this paper, we present an experimental investigation of electrokinetic transport in nanometer-scale channels with finite double layers. We investigate the accuracy and extent of application of Gouy–Chapman–Stern continuum theory<sup>17</sup> by making detailed comparisons between experiments and continuum theory. We experimentally validate the analytical model of our previous paper.<sup>16</sup> We also demonstrate a technique we term electrokinetic separation by ion valence (EKSIV), which can be used to determine both ion valence and mobility of analyte species from a comparison of micro- and nanoscale transport measurements.

## EXPERIMENTAL METHODS AND SETUP

**Channel Design and Fabrication.** We designed and fabricated a variety of both nanochannel and microchannel devices such as that shown in Figure 1. We fabricated various configurations including straight channels, simple crosses, and so-called double-T channel geometries. Straight channels had typical lengths of 36 mm and simple cross and double-T channel geometries channels all had a separation column length of 30 mm.

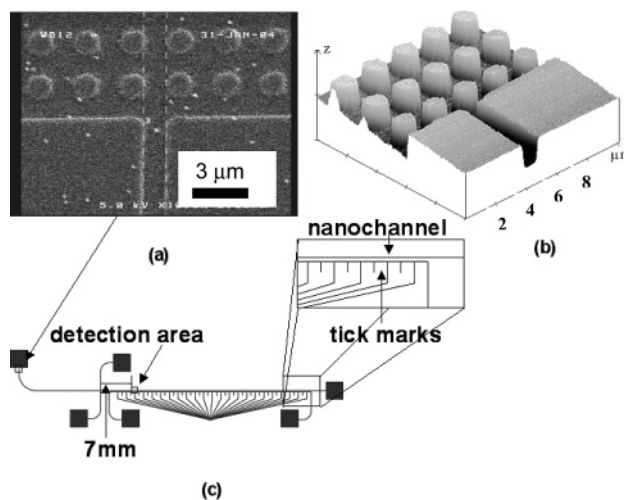


**Figure 1.** SEM (a) and AFM scan (b) of the inlet region of a nanometer-scale fluidic channel. The spots in the SEM image are an artifact of the metallization preprocessing of the sample. The vertical scale of the AFM (z-direction in the plot) is exaggerated by a factor of 20 for clarity of presentation (channel is 102 nm deep). The images show 1-mm-diameter posts near the inlet of the nanochannel which serve as an integrated filtering structure. (c) Schematic of nanochannel device with 125  $\mu\text{m}$  by 75  $\mu\text{m}$  detection area centered 7 mm from the injection point. Tick marks are etched below the nanochannel test section to aid in registration and quantitation.

Both the nanometer- and micrometer-scale fluidic channels were fabricated using conventional optical photolithography, dry chemical etching, and bonding techniques.<sup>18</sup> Figure 1 shows images from an atomic force microscope (AFM) and scanning electron microscopy (SEM) for a typical nanochannel system prior to bonding the cover plate. Channel depths of 2052, 102, and 38.5 nm were fabricated using this method and characterized by both AFM and SEM measurements. These channel depths will be referred to in this paper by the nominal values of 2  $\mu\text{m}$ , 100 nm, and 40 nm. Rms surface roughness as measured by AFM was  $\pm 0.2$  nm for all channel depths.

To seal the channel and provide fluidic interconnects, 1.5-mm-diameter through holes were created in a second fused-silica wafer using  $\text{CO}_2$  laser machining. Both wafers were hydrolyzed in  $\text{H}_2\text{SO}_4/\text{H}_2\text{O}_2$  at 80  $^\circ\text{C}$ , rinsed in deionized water, and mated, before a 5-h anneal at 1200  $^\circ\text{C}$ . Cylindrical plastic reservoirs were potted onto the substrate using epoxy. The channels are filled with deionized water by capillary action and stored wet for future use.

**Chemicals and Reagents.** Our aqueous, buffered solutions consisted of nine concentrations of sodium tetraborate buffer (Sigma Aldrich, St. Louis, MO), ranging from 0.1 to 10 mM and prepared using filtered deionized water (Fisher Scientific W2-20, Fairlawn, NJ). The pH of the buffered solutions varied between 7.9 and 9.2 depending on concentration as measured using a pH meter (Corning, Corning, NY), although the great majority of conditions resulted in pH values between 8.8 and 9.2. We filtered electrolyte solutions prior to experiments with 200-nm pore syringe filters (Nalgene Labware, Rochester, NY). We measured species velocities of three fluorescent analytes: rhodamine B (Acros Organics, Geel, Belgium), bodipy (Molecular Probes, Inc.), and

(13) Levine, S.; Marriott, J. R.; Robinson, K. J. *Chem. Soc., Faraday Trans. 2* **1974**, 71, 136.

(14) Levich, V. G. *Physicochemical Hydrodynamics*; Prentice-Hall: Englewood Cliffs, NJ, 1962.

(15) Probstein, R. F. *Physicochemical Hydrodynamics*, 2nd ed.; John Wiley and Sons: New York, 1994.

(16) Pennathur, S.; Santiago, J. *Anal. Chem.* **2005**, 77, 6772–6781. ac050835y

(17) Lyklema, J. *Fundamentals of Interfacial and Colloid Science*, 2; Academic Press: New York, 1995.

(18) Jacobson, S. C.; Moore, A. W.; Ramsey, J. M. *Anal. Chem.* **1995**, 67, 2059–2063.

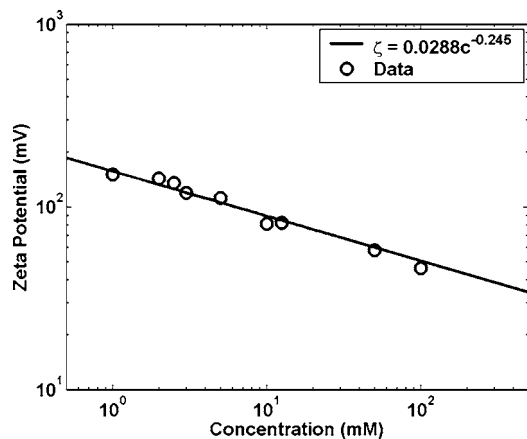


**Figure 2.** Values of  $\zeta$  determined from measurements of area-averaged velocities of neutral species and current monitoring measurements over buffer concentrations ranging from 1 to 100 mM. A power law fit shows parameter values  $a$  and  $b$  are equal to 0.0288 and  $-0.245$ , respectively.  $\zeta$  data shown for cases where EDL overlap is negligible.

fluorescein (Molecular Probes, Inc.). These analytes have respective valences of 0,  $-1$ , and  $-2$  at the pH range of interest.

**Current Monitoring.** To measure accurately area-averaged velocity, we performed both current monitoring<sup>19</sup> and electrokinetic injection experiments. Our experimental setups are similar to those of Oddy et al.<sup>20</sup> Current monitoring experiments were performed in straight channel devices following the method described by Sze.<sup>19</sup> In the case of thin-EDL, microchannel measurements, the area-averaged velocity and field can be used to directly provide a measure of  $\zeta$  potential using the Helmholtz–Smoluchowski relation.<sup>15</sup> The  $\zeta$  potentials obtained from these microchannel measurements were used to calibrate the substrate  $\zeta$  potential at each electrolyte concentration. In all cases, these independent  $\zeta$  potential measurements were for the same electrolyte chemistry used in the corresponding nanochannel case. These measurements are presented in Figure 2. Current monitoring experiments were also performed for nanoscale channels. This technique provides the mobility associated with an area average of the nonuniform velocity profiles of electroosmotic flows with finite EDLs (i.e., area-averaged velocity of liquid).

**Fluorescence Imaging.** We obtained species transport data using epifluorescence microscopy and CCD camera imaging. Image data were acquired using electrokinetic injections in cross- and double T-shaped nanochannel geometries. Electrical potentials were applied using platinum electrodes. We recorded epifluorescence images using an inverted epifluorescence microscope (Olympus IX70) fitted with a water immersion objective lens with a magnification of  $60\times$  and a numerical aperture of 1.0 (Olympus, Inc.). These images were used to track the speed and shape of injected bands. Images were recorded 7 mm downstream of the injection point using a cooled intensified CCD camera (I-PentaMAX, Gen III, Princeton Instruments) with a  $512 \times 512$  CCD pixel array and 12-bit digitization. The camera controller actuated a shutter in the illumination path to minimize photobleaching. Frame rates ranged from 5 to 200 ms depending on the depth of

the channel and type of analyte used. On-chip binning was used to increase signal-to-noise ratio. For quantitative analysis of the CCD images, a background image was subtracted from the raw image and this difference was normalized by the difference between a flat-field and a background image.<sup>21</sup> To compare the two-dimensional image data with the one-dimensional model, fluorescent intensity was averaged along the width of the channel to yield one-dimensional streamwise intensity profiles. Area-averaged velocity can thus be measured directly in these experiments using the relation  $\langle u \rangle = L/\Delta t$ , with  $\Delta t$  equaling the time from the electrokinetic injection to the time of maximum intensity at the detection volume a distance  $L$  downstream. Note that both the observable motion of neutral solute bands and the interface motion in a current monitoring experiment are a direct measurement of area-averaged velocity of liquids as the solutes in these flows are well within the Taylor dispersion regime where transverse diffusion time scales are much smaller than advection and electrophoretic time scales.<sup>22, 23</sup>

To minimize possible effects caused by adsorption of solute, current was measured simultaneously during all injection experiments using an electrometer (Keithley 6314, Keithley, Inc.). Four channels of an eight-channel, differential high-voltage power supply (Micralyne, Alberta, Canada) were used to apply potentials (0–6 kV) for experiments. Voltage schemes for loading and injection of the analytes in the cross-channel devices follow those developed by Bharadwaj et al.<sup>21</sup>

**Experimental Conditions.** Prior to the introduction of a new buffer concentration into a micro- or nanochannel, filtered deionized water was electroosmotically flushed through the channel for 1 h to minimize the effects of any contaminants (such as sample ions remaining from previous experiments). Following that, a second 20-min rinsing cycle was initiated at the new buffer condition. Between each realization at a single electrolyte condition, we monitored current in the channel and compared it to the net ion current of the previous realization. In some cases, we noticed a slight upward drift of base current values after  $\sim 10$  min of collecting data (repeatable increases of  $\sim 10\%$  over 30-min periods. This is despite the fact that the electroosmotic mobility values of the channels were relatively constant (within  $\sim 5\%$ ). This phenomenon has been elsewhere observed for microchannels<sup>24,25</sup> and has been attributed to changes in wall charge due to adsorption of solute to the wall<sup>24</sup> and slight pH changes caused by electrolysis.<sup>25</sup> In all cases, we monitored both the net resistance and ion mobility of both micro- and nanochannels carefully as a function of buffer chemistry and the time from which channels were filled.

In our parametric investigation, we recorded data for nine buffer concentrations spanning the range of 0.1–10 mM; channel depths of 40 nm, 100 nm, and 2  $\mu\text{m}$ ; and electric fields of 100, 250, and 500 V/cm. Seven buffer concentrations were used in current monitoring experiments, while all other experiments were performed at nine concentrations. Each experiment was repeated 3–15 realizations per chip to ensure repeatability across realiza-

(19) Sze, A. J. *Colloid Interface Sci.* **2003**, *261*, 402–410.

(20) Oddy, M. H.; Santiago, J. G.; Mikkelsen, J. C. *Anal. Chem.* **2001**, *73*, 5822–5832.

(21) Bharadwaj, R.; Santiago, J. G.; Mohammadi, B. *Electrophoresis* **2002**, *23*, 2729–2744.

(22) Taylor, G. I. *Proc. R. Soc. London, Ser. A* **1953**, *219*, 186–203.

(23) Aris, R. *Proc. R. Soc. London, Ser. A* **1956**, *235*, 67–77.

(24) Ross, D.; Locascio, L. *Anal. Chem.* **2003**, *75*, 1218–1220.

(25) Rodriguez, I.; Chandrasekhar, N. *Electrophoresis* **2005**, *26*, 1114–1121.

**Table 1. List of Experiments Performed<sup>a</sup>**

exp	depth (nm)	$E$ field (V/cm)	species	concns/repeats
CM	40	100		7, 5
CM	40	250		7, 15
CM	40	500		7, 5
CM	100	100		7, 5
CM	100	250		7, 10
CM	100	500		7, 5
CM	2000	100		7, 5
CM	2000	250		7, 10
CM	2000	500		7, 5
Inj	40	100	RB	9, 3
Inj	40	250	RB	9, 5
Inj	40	500	RB	9, 3
Inj	100	100	RB	9, 3
Inj	100	250	RB	9, 5
Inj	100	500	RB	9, 3
Inj	2000	100	RB	9, 3
Inj	2000	250	RB	9, 5
Inj	2000	500	RB	9, 3
Inj	40	100	BDP	9, 3
Inj	40	250	BDP	9, 5
Inj	40	500	BDP	9, 3
Inj	100	100	BDP	9, 3
Inj	100	250	BDP	9, 5
Inj	100	500	BDP	9, 3
Inj	2000	100	BDP	9, 3
Inj	2000	250	BDP	9, 5
Inj	2000	500	BDP	9, 3
Inj	40	100	CF	9, 4
Inj	40	250	CF	9, 5
Inj	40	500	CF	9, 5
Inj	100	100	CF	9, 4
Inj	100	250	CF	9, 4
Inj	100	500	CF	9, 5
Inj	2000	100	CF	9, 5
Inj	2000	250	CF	9, 5
Inj	2000	500	CF	9, 5
summary	40, 100, 2000	100, 250, 500	BDP, RB, CF	1322 exp.

<sup>a</sup> CM, current monitoring experiment; Inj, electrokinetic injection experiment; RB, rhodamine B (neutral); BDP, bodipy ( $z = -1$ ); CF, carboxyl fluorescein ( $z = -2$ ).

tions and chip systems. Multiple times also reduced statistical uncertainty of measured quantities. A summary of experiments and conditions is shown in Table 1. The fifth column entries labeled “concns/repeats” show respectively the number of buffer concentrations explored at each condition and the number of realizations per buffer concentration. For example, 35 and 105 experiments were performed at the conditions described by the first and second rows, respectively. The last row summarizes the chip systems, electric fields, species, and total number of experiments performed: 1322 experiments were carried out.

We used total channel conductance measurements and ion mobility data<sup>26</sup> to determine Debye thickness for each buffer concentration.

## EXPERIMENTAL RESULTS AND DISCUSSION

We here describe results from current monitoring and electrokinetic injection experiments. First, we present the results of our microchannel experiments-based quantitation of  $\zeta$  potential

versus buffer concentration. Second, we present measurements of background liquid transport (i.e., flow rate of aqueous solute) obtained from both current monitoring and electrokinetic injection of neutral species. Third, we present electrophoretic transport measurements of charged species. We end the section with a demonstration of our EKSIV method.

**$\zeta$  Potential Measurements in a Microchannel.** The model presented by Pennathur and Santiago<sup>16</sup> relies on measured values of  $\zeta$  potential as a boundary condition to the nanochannel flow field.<sup>27</sup> This “grounding” of the model on measured values of  $\zeta$  potential is necessary as  $\zeta$  potential is in general not predictable from first principles.<sup>27</sup>  $\zeta$  potential can be interpreted as an empirically determined property of the substrate/electrolyte interface that is a function of local ionic concentration and pH. In our nanochannel experiments, we hold pH relatively constant by using a chemical buffer with an ion density significantly higher than that of sample analytes. We then use variations of total ion concentration (and three channel depths) to effect variations of Debye length-to-channel height ratio,  $\lambda_D/h$ , where Debye length is defined as  $\lambda_D = (\epsilon kT / e^2 \sum_{i=1}^N z_i^2 n_i)^{1/2}$ . This experimental method allows us to vary through 15 values of  $\lambda_D/h$  values but forces us to vary zeta potential simultaneously with  $\lambda_D/h$ . To collapse these data and effectively calibrate our substrate/electrolyte interface, we assume a convenient power law for the buffer concentration dependence of  $\zeta$  potential:<sup>28</sup>

$$\zeta = ac^b \quad (4)$$

where  $c$  is the sum over all ionic species concentrations,  $c = \sum_{i=0}^N z_i c_i$ , and  $a$  and  $b$  are empirically determined parameters. We obtained the parameters of this  $\zeta$  potential correlation using quantitative current monitoring and neutral dye tracking measurement, both of which provide measurements of liquid flow rates in microchannels (i.e., thin EDL conditions). We measured  $\zeta$  over buffer concentrations ranging from 1 to 100 mM. The data are shown Figure 2 and show excellent agreement with parameter values of  $a = 0.0288$  and  $b = -0.245$ . These power law parameters agree fairly well with the measurements of, for example, Conlisk et al.<sup>29</sup>

Below, we shall use eq 4 to relate  $\zeta$  and  $\lambda_D$  and present modeling results consistent with our experimental method of varying both channel depth and buffer concentration.

**Liquid Transport.** We first present quantitative data for liquid flow in micro- and nanochannels. Figure 3 shows quantitative sample measurements of area-averaged liquid velocity,  $\langle u \rangle$ , obtained from electrokinetic injections of neutral markers and current monitoring experiments. Area-averaged velocity is shown as a function of Debye length,  $\lambda_D/h$ , for various values of  $\zeta^* = \zeta ze/kT$ , where  $\zeta^*$  is the nondimensionalized value of the  $\zeta$  potential, and  $kT/ze$  is thermal voltage.<sup>27</sup> Velocity is nondimensionalized by the Helmholtz–Smoluchowski velocity. Data are presented for both 40- and 100-nm-depth channels. Shown together with the data are numerical transport model predictions of  $\langle u \rangle / u_{HS}$  as a function

(27) Hunter, R. J. *Zeta Potential in Colloid Science: Principles and Applications*; Academic Press: New York, 1981.

(28) Bharadwaj, R.; Santiago, J. Submitted to *Anal. Chem.*

(29) Conlisk, A. T.; Hansford, D. J.; Zheng, Z. *Electrophoresis* **2003**, *24*, 3006–3017.

(26) Lide, D. R. *CRC Handbook of Chemistry and Physics*, 76 ed.; CRC Press: New York, 1995.

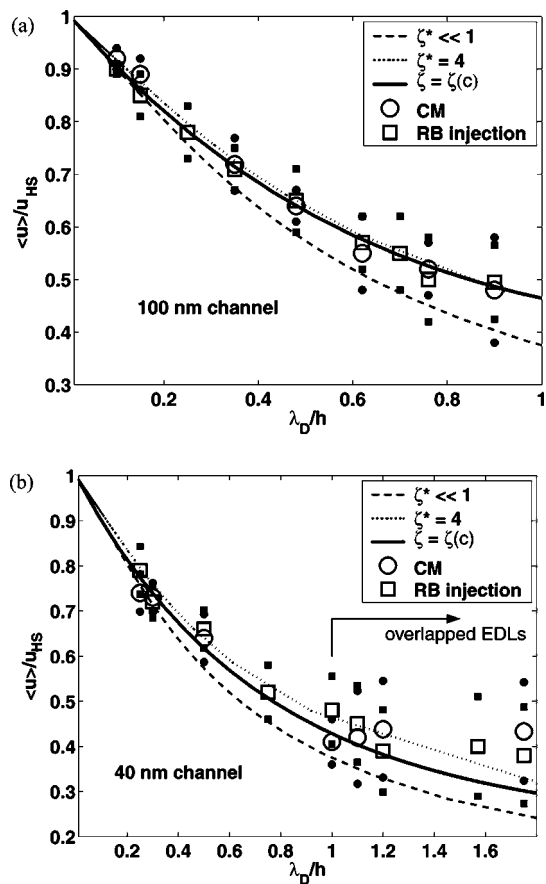


**Figure 3.** Area-averaged velocity normalized by the classical Helmholtz–Smoluchowski result for a thin EDL as a function of  $\lambda_D/h$  for (a) 100- and (b) 40-nm channels. Shown together with the data is a modeling result labeled  $\zeta(c)$  that uses eq 4 to relate  $\zeta$  to  $\lambda_D$ .  $\zeta^*$  values of this prediction ranged between 0.84 and 4.02, consistent with experiments. Also shown are modeling results for (constant)  $\zeta^*$  values of 1 and 4 as a reference. Area-averaged velocity decreases due to the velocity gradient caused by finite EDLs. Large open symbols in the plot are data, and smaller, closed symbols are corresponding error bars (e.g.,  $\bullet$  is the error bar symbol for  $\circ$ ). Error bars reflect 95% confidence intervals for the mean value of  $\sim 20$  realizations at each condition.

of  $\lambda_D$ . The most relevant of these predictions is the curve labeled  $\zeta(c)$ . This prediction uses eq 4 to relate  $\zeta$  to  $\lambda_D$  and therefore represents the best prediction of  $\langle u \rangle / u_{HS}$  for each experimentally realized value of  $\lambda_D/h$ . The  $\zeta^*$  values of this prediction ranged between 0.84 and 4.02, consistent with experiments. Numerical solutions for the cases of  $\zeta^* = 4$  and  $\zeta^* = 1$  are also shown as a reference.

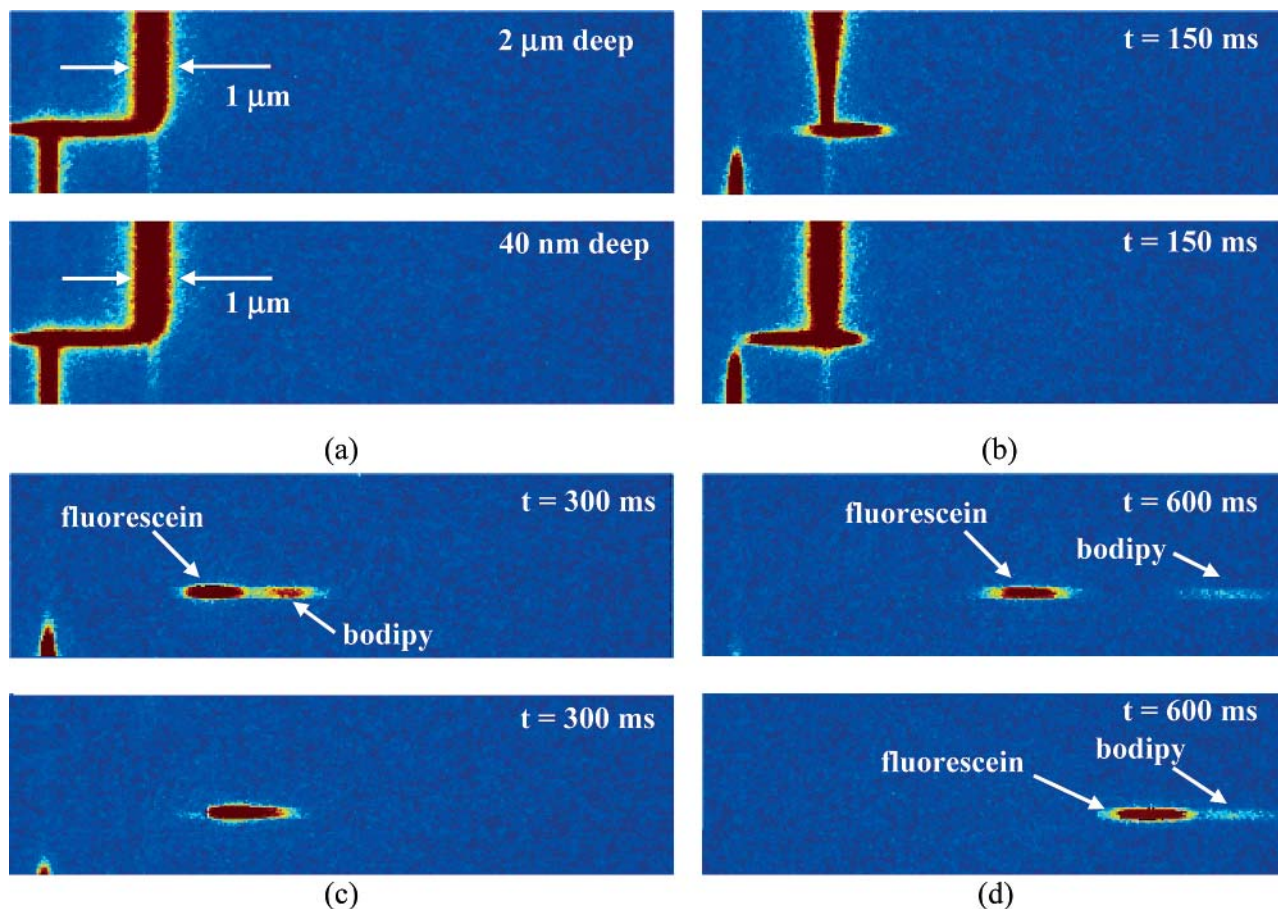
In Figure 3,  $\langle u \rangle / u_{HS}$  values near unity implies a thin EDL channel flow in which area-averaged velocity is approximately equal to the maximum velocity of the EDL. The drastic decrease of measured  $\langle u \rangle / u_{HS}$  with increasing  $\lambda_D/h$  clearly shows the flow deficit in a finite EDL flow. The  $\zeta(c)$  theory very well captures the variation of  $\langle u \rangle / u_{HS}$  versus  $\lambda_D/h$  for  $\lambda_D/h$  less than 1. Note that  $\zeta(c)$  here refers only to the  $\zeta$  versus concentration calibration of eq 4. The theory is therefore an excellent predictor of absolute values of  $\langle u \rangle / u_{HS}$  derived from first principles and an empirical calibration of  $\zeta$  obtained from independent experiments performed in a (thin EDL) microchannel. Continuum theory “grounded” on empirical calibration of the boundary condition for  $\zeta$  performs very well even for 40-nm channels.

Figure 3 also shows the excellent agreement between current monitoring and neutral dye injection experiments. This agreement provides strong validation that these techniques obtain consistent measurements of the same flow scale (area-averaged velocity). There is some disagreement between the two measurements and between measurements and theory at  $\lambda_D/h$  ratios larger than about unity. This discrepancy is expected as the value of  $\zeta$  potential for the overlapped EDL case is not precisely known. We should not expect that our  $\zeta$  calibration (and the value of  $u_{HS}$ ) should be accurate for the overlapped EDL regime as it was based on experiments with nonoverlapped EDLs.

Last, we note the error bars for data for 100-nm-depth channels are smaller than those of 40-nm channels at equivalent  $\lambda_D/h$  values. Measurements in 100-nm channels were more repeatable and consistent with theory than 40-nm channels. We believe relative surface roughness, not accounted for in the theory, may contribute to this slight difference between the two channel depths.

**Charged Species Transport.** We now present and discuss both qualitative and quantitative results for charged species transport in nanochannels and compare these to microchannel measurements. Figure 4 shows four successive fluorescence images of experimental data obtained using 2- $\mu\text{m}$ - and 40-nm-deep channels. Recall that the area-averaged liquid velocity in a 40-nm-deep channel is significantly smaller than that of a thin EDL channel at the same electric field and background electrolyte concentration. Since we are interested in a direct comparison of effective electrophoretic mobilities between micro- and nanochannels, we present here two cases with matched area-averaged liquid velocity. We accomplish this by using two background electrolyte concentrations (yielding two values of  $u_{HS}$ ). In microchannel device, we use 10 mM buffer, and in the 40-nm nanochannel we use a 1.46 mM buffer. At 25 V/cm, both channels show an area-averaged neutral species velocity of 25  $\mu\text{m/s}$ . We present results of electrokinetic injections and separations of 20  $\mu\text{M}$  carboxyl fluorescein ( $z_S = -2$ ) and 40  $\mu\text{M}$  bodipy ( $z_S = -1$ ). After 600 ms, the separation distance between the two analytes is lower for the nanochannel. This observation qualitatively supports the theory that transverse electromigration plays a key role in determining net streamwise transport of a charged solute. This coupling is clear from eq 3 as the area-averaging operation is clearly affected by the EDL potential distribution,  $\psi(y)$ . The fluxes of electromigration (away from the wall for a negative ion and negative wall charge) and diffusion result in an equilibrium ion distribution where  $z_S = -2$  ions are concentrated near the center of the channel and experience a velocity higher than that of the area-averaged liquid. The other analyte (bodipy) is also concentrated in the region near the channel center but to a lesser degree, as dictated by its lower valence of  $z_S = -1$ .

Next, we present quantitative measurements of electrophoretic transport in nanochannels and compare these to results from microchannels and theory. Figure 5 shows quantitative measurements of normalized area-averaged velocities of neutral and charged solutes in both 100- and 40-nm-deep channels. Here, measured velocity is normalized by first subtracting the expected usual electrophoretic (drift) velocity of the analyte ( $u_d = v_S z_S FE$ ) and then dividing this difference by  $u_{HS}$ . This scaling highlights the effects associated with the general coupling between net electrophoretic transport and the structure of the EDL. The



**Figure 4.** Sequence of epifluorescence images showing separations of 20  $\mu\text{M}$  carboxyl fluorescein ( $z_S = -2$ ) and 40  $\mu\text{M}$  bodipy ( $z_S = -1$ ) in devices with channel depths of 40 nm and 2  $\mu\text{m}$ . The top image of each pair is for a 1  $\mu\text{m}$  wide by 2  $\mu\text{m}$  deep channel filled with 10 mM sodium tetraborate buffer. The latter conditions result in an area-averaged liquid velocity of 25  $\mu\text{m/s}$ . The bottom image of each pair is for a channel 1  $\mu\text{m}$  wide and 40 nm deep filled with 1.5 mM sodium tetraborate buffer, resulting in an area-averaged liquid velocity of 24  $\mu\text{m/s}$ . Scalar images are taken (a) at injection ( $t = 0$ ), (b)  $t = 150$  ms, (c)  $t = 300$  ms, and (d)  $t = 600$  ms. In (d), the separation distance between the two analytes is lower for the nanochannel. This observation qualitatively supports the theory that transverse electromigration plays a key role in determining the net streamwise transport of a charged solute.

general retardation of the species velocities (for all three data sets in the figure) with increasing  $\lambda_D/h$  reflects the flow retardation associated with the finite-thickness EDL velocity profile. The dependence of the curves on species valence number directly reflects the coupling between transverse electromigration (and associated  $\psi(y)$  distribution) and streamwise electrophoretic flux. Note that the measurements of Figure 5 show a normalized area-averaged velocities for the neutral species that are consistently lower than those of the negatively charged species, as predicted by the model. Also, the  $z_S = -2$  consistently has a higher normalized velocity than the  $z_S = -1$  due its equilibrium concentration distribution, which is more tightly focused near the center of the channel.

Plotted along with the experimental data, Figure 5 shows theoretical predictions for corresponding experimental  $\lambda_D/h$  and  $\zeta$  potentials. There is very good agreement between the data and model predictions. For example, the model captures general effect of decreasing area-averaged electroosmotic velocity as  $\lambda_D/h$  increases. The model is able to capture the dependence of the scaled velocity on valence. This dependence on valence in these normalized coordinates is solely due to the effects of coupling between transverse electromigration and the nonuniform velocity profile, validating the model.

We can further demonstrate the effect of transverse electromigration and valence number on net streamwise electrophoresis by considering one other scaling of (specifically) the charged species data. We subtract theoretical values of area averaged velocity,  $\langle u \rangle$ , from the directly measured area-averaged velocities,  $\langle u_S \rangle$ , for charged species at each  $\lambda_D/h$ . We then nondimensionalize this difference by dividing by the electrophoretic drift velocity expected in a thin EDL channel,  $u_d$ . This normalization highlights contributions to the apparent electrophoretic mobility that are solely due to the coupling of the electromigrative flux and velocity. We call this quantity the nano-to-microelectrophoretic mobility ratio (see eq 3). Experimental data normalized in this fashion are shown together with numerical results in Figure 6. Again, we see the effects of ion valence due to the coupling between transverse electromigration and a nonuniform velocity profile. Figure 6 also shows that the experimental data achieve a maximum value of nano-to-micro mobility ratio at a value of  $\lambda_D/h$  between 0.40 and 0.47, depending on channel height and valence number. This maximum also coincides with the maximum difference between the two valence curves. For our system, these maximum values of  $\lambda_D/h$  represent the optimal condition for determining the effects of transverse electromigration and valence on net electrophoretic mobility.

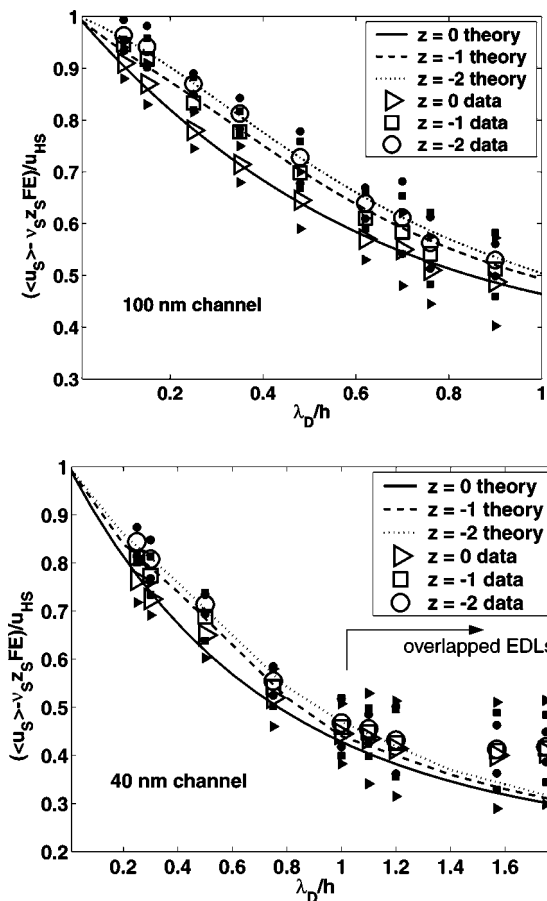


**Figure 5.** Area-averaged observed species velocity normalized using both electrophoretic drift velocity ( $u_d$ ) and Helmholtz–Smoluchowski velocity as a function of  $\lambda_D/h$ . Shown are results for a neutral analyte (rhodamine B), as well as bodipy ( $z_S = -1$ ) and fluorescein ( $z_S = -2$ ), together with predictions from the model. For nonoverlapped EDL conditions, the model captures both the major trend of  $\langle u_s \rangle - \nu_{S,S} FE / u_{HS}$  versus  $\lambda_D/h$ , as well as the valence dependence of the experimental results. Large open symbols in the plot are data, and smaller, closed symbols are corresponding, 95% confidence interval error bars for 5–25 realizations. (See Table 1.)

The results of Figure 6 allow us to experimentally demonstrate the idea of using micro- and nanochannel experiments as a so-called electrokinetic separation by ion valence method where we determine both mobility and valence of a charged analyte. The procedure for this method is summarized in our previous paper.<sup>16</sup> Briefly, we use our microchannel (thin EDL) experiments to determine the (typical) ion mobility of analytes. We then use a comparison such as that of Figure 6 to determine the valence of our charged analytes. To demonstrate this, we first obtained the ion mobilities of our analytes by analyzing the thin-EDL, microchannel experiments. These measured mobilities,  $\nu_S$ , were  $(-1.53 \pm 0.5) \times 10^{-4}$  and  $(-1.92 \pm 0.5) \times 10^{-4}$  (mol·s)/kg for fluorescein and bodipy, respectively (the uncertainties reflect 95% confidence intervals). These mobility values can be compared to the published values of  $(-1.76 \pm 0.5) \times 10^{-4}$ <sup>30</sup> and  $(-2.48 \pm 0.5) \times 10^{-4}$  (mol·s)/kg,<sup>21</sup> respectively.

Last, we conducted a comparison between experiments and data in which we treated analyte valence as an unknown. To this

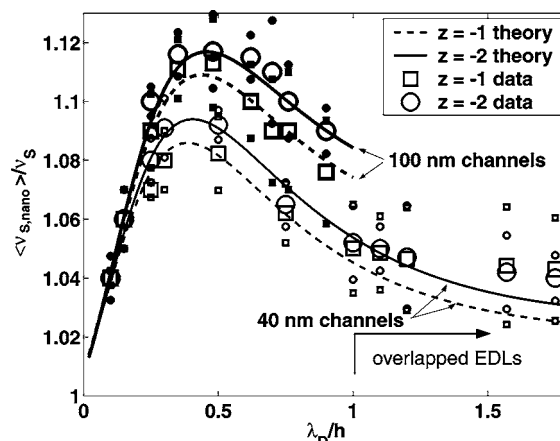


**Figure 6.** Comparison of measured effective mobility in a nanochannel (normalized by electrophoretic mobility as measured in a microchannel) versus model predictions for both 40- and 100-nm channels. Normalized mobility is shown as a function of  $\lambda_D/h$ . Large open symbols in the plot are data, and smaller, closed symbols are corresponding error bars. Error bars reflect 95% confidence on the mean of  $\sim 20$  realizations at each condition.

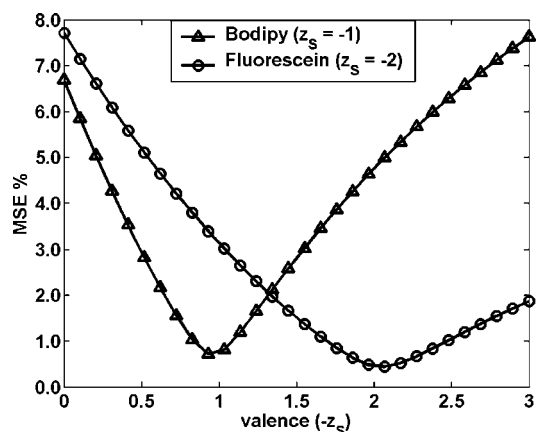


**Figure 7.** Mean square error as a function of valence for two charged analytes: fluorescein (published value of  $z_S = -2$ ) and bodipy (published value of  $z_S = -1$ ). Plots are generated by treating valence number of the experimental data for the two analytes as an unknown. Computed mean square error between experiments and model predictions for 100 values of valence between 0.01 and 3. Mean square error is minimized at values of  $z_S = -1.03$  for bodipy and  $z_S = -2.08$  for fluorescein, respectively. The respective regression coefficient for these nonlinear regressions are 0.993 and 0.995, respectively.

end, we first generated model predictions for 100 (real number) values of valence number spanning the range  $-0.01$  to  $-3.0$ . We then used a nearest-neighbor linear interpolation to predict solutions for intermediate valence numbers and generated a “library” of 1000 predictions of  $\langle \nu_{S,nano} \rangle / \nu_S$ . We then compared our experimental data for  $\langle \nu_{S,nano} \rangle / \nu_S$  (in the  $\lambda_D/h$  range between 0.3 and 1.0) to these predictions. This comparison was performed as a nonlinear regression analysis where we calculate mean square error between experimental data and theory for each possible valence number. The results are shown in Figure 7. The minimum mean square error for each analyte yielded an estimate of the most likely valence number of our analytes. This process is equivalent to fitting the model to the data by treating valence number as a fitting parameter that minimizes mean square error of  $\langle \nu_{S,nano} \rangle / \nu_S$ . The mean square error minimums of Figure 7

(30) Harrison, D.; Manz, A.; Fan, Z.; Ludi, H.; Widmer, H. *Anal. Chem.* **1992**, *64*, 1926–1932.

yielded valence fit values of  $z_S = -1.03$  for bodipy measurements and  $z_S = -2.08$  for fluorescein measurements. The regression coefficient values of these fits were 0.993 and 0.995, respectively. Assuming the valences are integers, the results are unambiguous. These measured valence values can be compared to the well-established, published values of  $-1$  and  $-2$ , for the two analytes.<sup>31</sup>

## CONCLUSIONS

We have presented an experimental study of electrokinetic transport of both charged and uncharged analytes in custom-fabricated nanochannels in fused-silica substrates. We used current monitoring and epifluorescence imaging to obtain measurements of area-averaged velocity of liquid streams,  $\langle u \rangle$ , and the observed streamwise velocity of charged species,  $\langle u_S \rangle$ . We then performed a parametric experimental study in an effort to yield insight into finite EDL effects and to study the applicability of continuum theory to nanoscale electrokinetic systems. We varied applied electric field, channel depth, background electrolyte concentration, and species valence to impose variations on  $\zeta$  potential, effective mobility, and  $\lambda_D/h$ .

Experimental results are in good agreement with continuum-based transport simulations and an analytical model presented in the first of this two-paper series. Our results demonstrate that area-averaged velocity of electroosmotic flow decreases strongly for increasing  $\lambda_D/h$ . The excellent agreement between data for

charged analytes and the model for nonoverlapped EDL conditions shows that net streamwise transport (and associated electrophoretic separations) depends on ion valence, ion mobility,  $\zeta$  potential, and Debye layer thickness. This dependence is a result of the coupling between transverse electromigration in the channel and the net streamwise transport that results from both electromigration and advection. Finally, we demonstrated the efficacy of a technique we term electrokinetic separation by ion valence. This technique enables the determination of both valence and mobility of an analyte from comparisons of micro- and nanochannel electrophoresis experiments. We applied EKSIV and determined the valences of bodipy and fluorescein unequivocally. Future work will include detailed studies of solute dispersion in nanoscale systems, as well as further quantitation and application of the EKSIV technique.

## ACKNOWLEDGMENT

This work is sponsored by the National Institutes of Health (Grant N01-HV-28183) and by a National Science Foundation PECASE Award (J.G.S., CTS-0239080-001) with Dr. Michael W. Plesniak as grant monitor.

Received for review May 13, 2005. Accepted August 19, 2005.

AC0508346

(31) Sjoback, R.; Nygren, J.; Kubista, M. *Spectrochim. Acta, Part A* **1995**, *51*, L7–21.